A third-order compact gas-kinetic scheme on unstructured meshes for compressible Navier–Stokes solutions

Liang Pan [a], Kun Xu [a,b,*]

[a] Department of Mathematics, Hong Kong University of Science and Technology, Clear Water Bay, Kowloon, Hong Kong
[b] Department of Mechanical and Aerospace Engineering, Hong Kong University of Science and Technology, Clear Water Bay, Kowloon, Hong Kong

A R T I C L E   I N F O

A B S T R A C T

In this paper, for the first time a third-order compact gas-kinetic scheme is proposed on unstructured meshes for the compressible viscous flow computations. The possibility to design such a third-order compact scheme is due to the high-order gas evolution model, where a time-dependent gas distribution function at cell interface not only provides the fluxes across a cell interface, but also presents a time accurate solution for flow variables at cell interface. As a result, both cell averaged and cell interface flow variables can be used for the initial data reconstruction at the beginning of next time step. A weighted least-square procedure has been used for the initial reconstruction. Therefore, a compact third-order gas-kinetic scheme with the involvement of neighboring cells only can be developed on unstructured meshes. In comparison with other conventional high-order schemes, the current method avoids the Gaussian point integration for numerical fluxes along a cell interface and the multi-stage Runge–Kutta method for temporal accuracy. The third-order compact scheme is numerically stable under CFL condition CFL $\approx$ 0.5. Due to its multidimensional gas-kinetic formulation and the coupling of inviscid and viscous terms, even with unstructured meshes, the boundary layer solution and vortex structure can be accurately captured by the current scheme. At the same time, the compact scheme can capture strong shocks as well.

1. Introduction

In computational fluid dynamics, the second-order methods are generally robust and reliable, and they are routinely employed in the practical computations. For the same computational cost, the higher-order methods can theoretically provide more accurate solutions, but they are less robust and more complicated. In recent decades, there have been continuous interests and efforts on the development of higher-order schemes. For engineering applications, the construction of higher-order numerical schemes on unstructured meshes becomes extremely demanding. There are a gigantic amount of publications about the introduction and survey of higher-order schemes. The current paper will mainly concentrate on the construction of third-order compact gas-kinetic scheme on unstructured meshes.

The gas-kinetic scheme (GKS) has been developed systematically for the compressible flow computations [25,26,14,10]. An evolution process from kinetic scale to hydrodynamic scale has been constructed for the flux evaluation. The kinetic

* Corresponding author at: Department of Mathematics, Hong Kong University of Science and Technology, Clear Water Bay, Kowloon, Hong Kong.
E-mail addresses: panliangjlu@sina.com (L. Pan), makxu@ust.hk (K. Xu).

effect through particle free transport contributes to the capturing of shock waves, and the hydrodynamic effect plays a dominant role for the capturing of resolved viscous and heat conducting solutions. In other words, the highly non-equilibrium gas distribution function in discontinuous region provides a physically consistent mechanism in the construction of numerical shock structure. In this sense, the gas-kinetic scheme is close to the upwind approach with implicit artificial dissipation, but with a different dissipative mechanism. In smooth flow region, the hydrodynamic scale physics corresponding to the multi-dimensional central difference discretization is automatically used for the capturing of viscous solutions. Due to the coupling of inviscid and viscous terms in the kinetic formulation, theoretically there is no fundamental barrier for the finite volume gas-kinetic scheme to capture Navier–Stokes solutions with structured or unstructured meshes. With the discretization in particle velocity space, a unified gas-kinetic scheme has been developed for the transport process in the entire flow regime from rarefied to continuum ones [27,18,9,23].

Recently, with the incorporation of higher-order initial data reconstruction, a higher-order gas-kinetic scheme has been proposed in [16,15,17]. The flux evaluation is based on the time evolution of flow variables from initial piece-wise discontinuous polynomials (parabolas) around a cell interface, where the spatial and temporal derivatives of gas distribution function are coupled nonlinearly. The distributions of flow variables around a cell interface interact through particle transport and collision in the determination of flux function. Besides the evaluation of a time-dependent flux function across a cell interface, the third-order gas evolution model provides an accurate time-dependent cell interface solution for flow variables as well. Thus, it is feasible to develop a compact scheme with the consideration of both cell averaged and point-wise cell interface values. A compact third-order gas-kinetic scheme has been proposed recently for the compressible Euler and Navier–Stokes equations on structured meshes with WENO-type reconstruction [21]. However, this reconstruction technique is difficult to be extended to unstructured meshes. Therefore, in this paper, a weighted least-square reconstruction will be used on unstructured meshes. To the third-order accuracy, a quadratic distribution for the flow variables inside each cell needs to be determined. Based on the cell averaged and cell interface values from neighboring cells only, an over-determined linear system is formed. With the weighted least-square solution for this system, the whole flow distribution can be fully determined. The shock detector can be used as well to switch between higher-order (3rd) and lower order (2nd) reconstructions in different regions. In comparison with traditional schemes, the Gaussian point integration for flux evaluation along a cell interface and the multi-stage Runge–Kutta method for temporal accuracy are avoided in the current compact scheme. At the same time, the third-order compact scheme is stable under the CFL condition CFL ≈ 0.5.

This paper is organized as follows. In Section 2, the finite volume scheme on unstructured meshes and third-order gas-kinetic flux solver are introduced. In Section 3, the compact reconstruction on unstructured meshes is presented. Section 4 includes numerical examples to validate the current algorithm. The last section is the conclusion.

2. Finite volume gas-kinetic scheme

2.1. Finite volume scheme on unstructured meshes

The two-dimensional gas-kinetic BGK equation [3] can be written as

$$f_t + \mathbf{u} \cdot \nabla f = \frac{g - f}{\tau}, \tag{1}$$

where f is the gas distribution function, g is the corresponding equilibrium state, and τ is the collision time. The collision term satisfies the following compatibility condition

$$\int \frac{g - f}{\tau} \varphi d\Xi = 0, \tag{2}$$

where $\varphi = (1, u, v, \frac{1}{2}(u^2 + v^2 + \xi^2))$, $d\Xi = du dv d\xi_1 \dots d\xi_K$, K is the number of internal degree of freedom, i.e. $K = (4 - 2\gamma)/(\gamma - 1)$ for two-dimensional flows, and γ is the specific heat ratio.

Based on the Chapman–Enskog expansion of BGK model, the Euler and Navier–Stokes, Burnett, and super-Burnett equations can be derived [4,19,25]. In the smooth region, the gas distribution function can be expanded as

$$f = g - \tau D_{\mathbf{u}} g + \tau D_{\mathbf{u}} (\tau D_{\mathbf{u}}) g - \tau D_{\mathbf{u}} [\tau D_{\mathbf{u}} (\tau D_{\mathbf{u}}) g] + \dots,$$

where $D_{\mathbf{u}} = \partial/\partial t + \mathbf{u} \cdot \nabla$. By truncating on different orders of τ, the corresponding macroscopic equations can be derived. For the Euler equations, the zeroth order truncation is taken, i.e. $f = g$. For the Navier–Stokes equations, the first order truncation is

$$f = g - \tau(u g_x + v g_y + g_t). \tag{3}$$

Based on the higher order truncations, the Burnett and super-Burnett equations can be also derived.

In this section, the control volumes are simply triangles. For each control volume Ω_i, its boundary is given by three line segments

$$\partial \Omega_i = \bigcup_m \Gamma_{im}.$$

Thus, taking moments of the kinetic equation (1) and integrating with respect to time and space, the finite volume scheme can be expressed as

$$W_i^{n+1} = W_i^n - \frac{1}{|\Omega_i|} \int\limits_{t^n}^{t^{n+1}} \sum_m F_{im}(t) dt, \tag{4}$$

where $W = (\rho, \rho U, \rho V, \rho E)$ are the conservative variables, $F_{im}(t) = (F_\rho, F_{\rho u}, F_{\rho v}, F_E)$ are the fluxes across the cell interface Γ_{im} in the global coordinate, which are defined as

$$F_{im}(t) = \int\limits_{\Gamma_{im}} (\int \varphi f(x, y, t, u, v, \xi) \mathbf{u} \cdot \mathbf{n} du dv d\xi) ds, \tag{5}$$

where $\mathbf{n} = (\cos\theta, \sin\theta)$ is the outer normal direction of Γ_{im}, and the tangential direction is denoted as $\mathbf{t} = (-\sin\theta, \cos\theta)$. Eq. (4) is a discrete conservation law, which is valid in any scale if the interface fluxes are properly defined. This equation is beyond the validity of Navier–Stokes equations.

According to the coordinate transformation, the local coordinate of Γ_{im} is expressed as $(\widetilde{x}, \widetilde{y}) = (0, \widetilde{y})$, where $\widetilde{y} \in [-d, d]$ and $d = |\Gamma_{im}|/2$, and the velocities in the local coordinate are given by

$$\begin{cases} \widetilde{u} = u\cos\theta + v\sin\theta, \\ \widetilde{v} = -u\sin\theta + v\cos\theta. \end{cases} \tag{6}$$

For the gas distribution function in the local coordinate, $\widetilde{f}(\widetilde{x}, \widetilde{y}, t, \widetilde{u}, \widetilde{v}, \xi) = f(x, y, t, u, v, \xi)$ and $du dv = d\widetilde{u} d\widetilde{v}$, then the line integration for the gas distribution function over the cell interface Γ_{im} can be transformed as

$$\int\limits_{\Gamma_{im}} \int \varphi f(x, y, t, u, v, \xi) \mathbf{u} \cdot \mathbf{n} du dv d\xi ds = \int\limits_{-d}^{d} \int \varphi \widetilde{f}(0, \widetilde{y}, t, \widetilde{u}, \widetilde{v}, \xi) \widetilde{u} d\widetilde{u} d\widetilde{v} d\xi d\widetilde{y}. \tag{7}$$

Thus, in the computation, the numerical fluxes in the local coordinate $\widetilde{F}(t) = (F_{\widetilde{\rho}}, F_{\widetilde{m}}, F_{\widetilde{n}}, F_{\widetilde{E}})$ are obtained firstly by taking moments of the gas distribution function in the local coordinate

$$\widetilde{F}(t) = \int\limits_{-d}^{d} \int \widetilde{u} \widetilde{\varphi} \widetilde{f}(0, \widetilde{y}, t, \widetilde{u}, \widetilde{v}, \xi) d\widetilde{u} d\widetilde{v} d\xi d\widetilde{y}, \tag{8}$$

where $\widetilde{\varphi} = (1, \widetilde{u}, \widetilde{v}, \frac{1}{2}(\widetilde{u}^2 + \widetilde{v}^2 + \xi^2))$. According to Eq. (6) and Eq. (7), the fluxes in the global coordinate can be expressed as a combination of the fluxes in the local coordinate

$$\begin{cases} F_\rho = F_{\widetilde{\rho}}, \\ F_m = F_{\widetilde{m}}\cos\theta - F_{\widetilde{n}}\sin\theta, \\ F_n = F_{\widetilde{m}}\sin\theta + F_{\widetilde{n}}\cos\theta, \\ F_E = F_{\widetilde{E}}. \end{cases} \tag{9}$$

With the above numerical fluxes at cell interface, the flow variables inside each control volume can be updated according to Eq. (4).

2.2. Gas-kinetic flux solver

In this section, the numerical flux will be presented in the local coordinate. For simplicity, all notations with tilde will be omitted hereafter. In order to simulate the Navier–Stokes solutions, we need to model the interface flux function. For the gas distribution function at a cell interface, the integral solution of BGK equation Eq. (1) in the local coordinate can be written as

$$f(0, y, t, u, v, \xi) = \frac{1}{\tau} \int\limits_0^t g(x', y', t', u, v, \xi) e^{-(t-t')/\tau} dt' + e^{-t/\tau} f_0(-ut, y - vt, u, v, \xi), \tag{10}$$

where $x = 0$ is the location of cell interface, $x = x' + u(t - t')$ and $y = y' + v(t - t')$ are the trajectory of particles, f_0 is the initial gas distribution function, and g is the corresponding equilibrium state.

To construct a multidimensional third-order gas-kinetic solver, the following notations are introduced firstly

$$a_1 = (\partial g/\partial x)/g, a_2 = (\partial g/\partial y)/g, A = (\partial g/\partial t)/g, B = (\partial A/\partial t),$$

$$d_{11} = (\partial a_1/\partial x), d_{12} = (\partial a_1/\partial y) = (\partial a_2/\partial x), d_{22} = (\partial a_2/\partial y),$$

$$b_1 = (\partial a_1/\partial t) = (\partial A/\partial x), b_2 = (\partial a_2/\partial t) = (\partial A/\partial y),$$

where g is an equilibrium state. The dependence of these coefficients on particle velocity can be expanded as the following form [26]

$$a_1 = a_{11} + a_{12}u + a_{13}v + a_{14}\frac{1}{2}(u^2 + v^2 + \xi^2),$$

$$\cdots$$

$$B = B_1 + B_2u + B_3v + B_4\frac{1}{2}(u^2 + v^2 + \xi^2).$$

For the kinetic part of the integral solution Eq. (10), the gas distribution function can be constructed as

$$f_0 = f_0^l(x, y, u, v)H(x) + f_0^r(x, y, u, v)(1 - H(x)), \tag{11}$$

where $H(x)$ is the Heaviside function, f_0^l and f_0^r are the initial gas distribution functions on both sides of a cell interface, which have one to one correspondence with the initially reconstructed polynomials of macroscopic flow variables on both sides of cell interface. To construct a third-order scheme, the Taylor expansion for the gas distribution function in space at $(x, y) = (0, 0)$ is expressed as

$$f_0^k(x, y) = f_G^k(0, 0) + \frac{\partial f_G^k}{\partial x}x + \frac{\partial f_G^k}{\partial y}y + \frac{1}{2}\frac{\partial^2 f_G^k}{\partial x^2}x^2 + \frac{\partial^2 f_G^k}{\partial x \partial y}xy + \frac{1}{2}\frac{\partial^2 f_G^k}{\partial y^2}y^2,$$

where $k = l, r$. For the Euler equations, $f_G^k = g_k$ and the kinetic part of Eq. (10) can be obtained. For the Navier–Stokes equations, according to Eq. (3) and the notations introduced above, the gas distribution function is

$$f_G^k = g_k - \tau(a_{1k}u + a_{2k}v + A_k)g_k,$$

where g_l, g_r are the equilibrium states corresponding to the macroscopic variables W_l, W_r, which will be given by the reconstruction procedure at both sides of cell interface in the following section. Thus, the corresponding kinetic part of Eq. (10) can be written as

$$e^{-t/\tau}f_0^k(-ut, y - vt, u, v)$$

$$= C_7 g_k[1 - \tau(a_{1k}u + a_{2k}v + A_k)]$$

$$+ C_8 g_k[a_{1k}u - \tau((a_{1k}^2 + d_{11k})u^2 + (a_{1k}a_{2k} + d_{12k})uv + (A_k a_{1k} + b_{1k})u)]$$

$$+ C_8 g_k[a_{2k}v - \tau((a_{1k}a_{2k} + d_{12k})uv + (a_{2k}^2 + d_{22k})v^2 + (A_k a_{2k} + b_{2k})v)]$$

$$+ C_7 g_k[a_{2k} - \tau((a_{1k}a_{2k} + d_{12k})u + (a_{2k}^2 + d_{22k})v + (A_k a_{2k} + b_{2k}))]y$$

$$+ \frac{1}{2}C_7 g_k[(a_{1k}^2 + d_{11k})(-ut)^2 + 2(a_{1k}a_{2k} + d_{12k})(-ut)(y - vt) + (a_{2k}^2 + d_{22k})(y - vt)^2], \tag{12}$$

where the coefficients $a_{1k}, \ldots, A_k, k = l, r$ are defined according to the expansion of g_k.

After determining the kinetic part f_0, the equilibrium state g in the integral solution Eq. (10) can be expanded in space and time as follows

$$g = g_0 + \frac{\partial g_0}{\partial x}x + \frac{\partial g_0}{\partial y}y + \frac{\partial g_0}{\partial t}t + \frac{1}{2}\frac{\partial^2 g_0}{\partial x^2}x^2 + \frac{\partial^2 g_0}{\partial x \partial y}xy + \frac{1}{2}\frac{\partial^2 g_0}{\partial y^2}y^2 + \frac{1}{2}\frac{\partial^2 g_0}{\partial t^2}t^2 + \frac{\partial^2 g_0}{\partial x \partial t}xt + \frac{\partial^2 g_0}{\partial y \partial t}yt, \tag{13}$$

where g_0 is the equilibrium state located at interface, which can be determined through the compatibility condition Eq. (2)

$$\int \varphi g_0 d\Xi = W_0 = \int_{u>0} \varphi g_l d\Xi + \int_{u<0} \varphi g_r d\Xi, \tag{14}$$

where W_0 are the macroscopic variables corresponding the equilibrium state g_0. Based on the Taylor expansion for the equilibrium state Eq. (13), the hydrodynamic part in Eq. (10) can be written as

$$\frac{1}{\tau} \int_0^t g(x', y', t', u, v) e^{-(t-t')/\tau} dt'$$

$$= C_1 g_0 + C_2 g_0 \bar{a}_1 u + C_2 g_0 \bar{a}_2 v + C_1 g_0 \bar{a}_2 y + C_3 g_0 \overline{A}$$

$$+ \frac{1}{2} C_4 g_0 (\bar{a}_1^2 + \bar{d}_{11}) u^2 + C_6 g_0 (\overline{A} \bar{a}_1 + \bar{b}_1) u + \frac{1}{2} C_5 g_0 (\overline{A}^2 + \overline{B})$$

$$+ \frac{1}{2} C_1 g_0 (\bar{a}_2^2 + \bar{d}_{22}) y^2 + C_2 g_0 (\bar{a}_2^2 + \bar{d}_{22}) v y + \frac{1}{2} C_4 g_0 (\bar{a}_2^2 + \bar{d}_{22}) v^2$$

$$+ C_2 g_0 (\bar{a}_1 \bar{a}_2 + \bar{d}_{12}) u y + C_4 g_0 (\bar{a}_1 \bar{a}_2 + \bar{d}_{12}) u v$$

$$+ C_3 g_0 (\overline{A} \bar{a}_2 + \bar{b}_2) y + C_6 g_0 (\overline{A} \bar{a}_2 + \bar{b}_2) v, \tag{15}$$

where the coefficients $\bar{a}_1, \bar{a}_2, \ldots, \overline{A}, \overline{B}$ are defined from the expansion of equilibrium state g_0. The coefficients $C_i, i = 1, \ldots, 8$ in Eq. (15) and Eq. (12) are given by

$$C_1 = 1 - e^{-t/\tau}, C_2 = (t + \tau) e^{-t/\tau} - \tau, C_3 = t - \tau + \tau e^{-t/\tau}, C_4 = -(t^2 + 2t\tau) e^{-t/\tau},$$

$$C_5 = t^2 - 2t\tau, C_6 = -t\tau (1 + e^{-t/\tau}), C_7 = e^{-t/\tau}, C_8 = -t e^{-t/\tau}.$$

Substituting Eq. (15) and Eq. (12) into the integral solution Eq. (10), the gas distribution function at the cell interface can be obtained. The superscripts or subscripts of coefficients $a_1, a_2, \ldots, A, B$ in Eq. (12) and Eq. (15) are omitted for simplicity and they can be determined by the spatial derivatives of macroscopic flow variables and the compatibility condition as follows [15]

$$
\begin{cases}
\langle a_1 \rangle = \dfrac{\partial W}{\partial x}, \langle a_2 \rangle = \dfrac{\partial W}{\partial y}, \langle A + a_1 u + a_2 v \rangle = 0, \\[2mm]
\langle a_1^2 + d_{11} \rangle = \dfrac{\partial^2 W}{\partial x^2}, \langle a_2^2 + d_{22} \rangle = \dfrac{\partial^2 W}{\partial y^2}, \langle a_1 a_2 + d_{12} \rangle = \dfrac{\partial^2 W}{\partial x \partial y}, \\[2mm]
\langle (a_1^2 + d_{11}) u + (a_1 a_2 + d_{12}) v + (A a_1 + b_1) \rangle = 0, \\[2mm]
\langle (a_1 a_2 + d_{12}) u + (a_2^2 + d_{22}) v + (A a_2 + b_2) \rangle = 0, \\[2mm]
\langle (A a_1 + b_1) u + (A a_2 + b_2) v + (A^2 + B) \rangle = 0,
\end{cases}
\tag{16}
$$

where $< \ldots >$ are the moments of gas distribution function, and defined by

$$< \ldots > = \int \varphi g(\ldots) d\Xi.$$

In the following section, with the reconstruction procedure, the conservative values W_l, W_r and W_0 at the center of cell interface corresponding to the equilibrium g_l, g_r, g_0 and the corresponding derivatives in Eq. (16) will be presented.

3. Compact reconstruction

This paper focuses on the development of third-order compact finite volume scheme. In the traditional schemes, in order to achieve the higher-order accuracy, the reconstruction of higher-order polynomials for macroscopic flow variables inside each cell is needed as the initial condition at the beginning of each time step. For the higher-order reconstruction, a large stencil is usually needed to determine all degrees of freedom through the WENO or least square techniques [1,7,6,2,20]. Specifically, the non-compact stencil for third-order reconstruction is shown in Fig. 1.

In this section, the reconstruction will be done on the unstructured meshes with a compact stencil, which is shown in Fig. 2. For simplicity, the whole reconstruction procedure is performed in a local coordinate (x, y) relative to the cell interface AB as shown in Fig. 2. It is consistent with the evaluation of time-dependent gas distribution function at cell interface.

In the gas-kinetic scheme, besides the numerical fluxes, the macroscopic point-wise values at cell interface in the local coordinate can be obtained by taking moments of gas distribution function

$$W(t, y) = \int \varphi f(x_{i+1/2}, y, t, u, v, \xi) \, du \, dv \, d\xi. \tag{17}$$

As shown in the last section, the whole polynomials for macroscopic variables will participate the flow evolution, and the spatial and temporal derivatives of gas distribution function are coupled nonlinearly. This point-wise value at the cell interface Eq. (17) is a solution of gas evolution model, which can be used in the reconstruction stage at the beginning of next time step. Thus, in the following, a third-order compact reconstruction will be presented on unstructured meshes, in which both cell averaged values and point-wise cell interface values shown in Fig. 2 will be used in the spatial reconstruction.
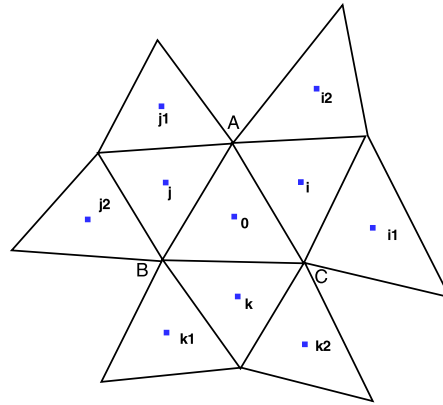
Fig. 1. The stencil for non-compact reconstruction for triangle $\Omega_0 = \triangle_{ABC}$. The blue squares represent the cell averaged values of control volume. (For interpretation of the references to color in this figure legend, the reader is referred to the web version of this article.)
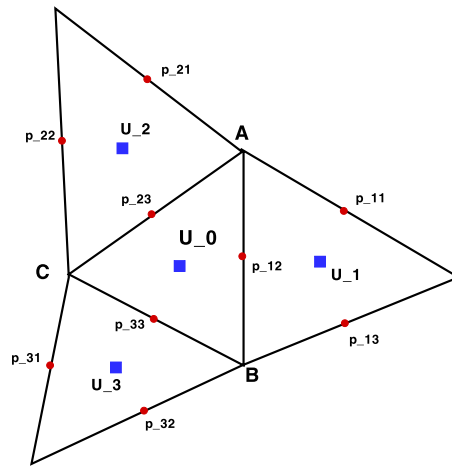

Fig. 2. The stencil of a compact reconstruction for triangle $\Omega_0 = \triangle_{ABC}$. The blue squares are the cell averaged values and the red circles are point values at the center of cell interface. (For interpretation of the references to color in this figure, the reader is referred to the web version of this article.)

The macroscopic variables for reconstruction are denoted by U. For the smooth flow, the conservative variables W will be directly used for reconstruction, i.e. $U = W$. For the flow with discontinuity, in order to eliminate the spurious oscillation and improve the stability, the compact reconstruction is based on the characteristic variables. Denote $F(W) = (\rho U, \rho U^2 + p, \rho U V, U(\rho E + p))$ in the local coordinate. The Jacobian matrix $\partial F / \partial W$ can be diagonalized by the right eigenmatrix R. For a specific cell interface, R_* is the right eigenmatrix of $\partial F / \partial W^*$, and W^* are the averaged conservative values from both side of cell interface. The variables for reconstruction are defined as $U = R_*^{-1} W$.

To the third-order accuracy, the expansion of macroscopic variable U inside the cell Ω_0 can be expressed as

$$U(x, y) = U_0 + U_x((x - x_0) - \widehat{x_0}) + U_y((y - y_0) - \widehat{y_0}) + \frac{1}{2} U_{xx}((x - x_0)^2 - \widehat{x_0^2})$$

$$+ U_{xy}((x - x_0)(y - y_0) - \widehat{x_0 y_0}) + \frac{1}{2} U_{yy}((y - y_0)^2 - \widehat{y_0^2}), \tag{18}$$

where (x_0, y_0) is the barycenter of Ω_0, U_0 is the cell averaged value for $U(x, y)$ over Ω_0, and

$$\widehat{x^m y^n} = \frac{1}{|\Omega_0|} \int_{\Omega_0} (x - x_0)^m (y - y_0)^n dV.$$

The cell averaged value for the base function over the triangle Ω_i is denoted as

$$\widehat{x^m y^n}_i = \frac{1}{|\Omega_i|} \int_{\Omega_i} ((x - x_0)^m (y - y_0)^n - \widehat{x^m y^n}) dV. \tag{19}$$

The point-wise value for the base function at the point $p_{ij} = (x_{ij}, y_{ij})$ is denoted as

$$x^m y^n_{ij} = ((x_{ij} - x_0)^m (y_{ij} - y_0)^n - \widehat{x^m y^n}). \tag{20}$$

3.1. Initial data reconstruction

In this subsection, the weighted least-square reconstruction will be presented for the initial data reconstruction. As shown in Fig. 2, three cell averaged values $U_i, i = 1, 2, 3$ (blue square) from the neighboring cells and nine point-wise values $U_{ij}, i, j = 1, 2, 3$ (red circle) from the cell interface will be used.

For the third-order expansion, with the definition of cell averaged and point-wise values for the base function Eq. (19) and Eq. (20), we have

$$U_x \widehat{x}_i + U_y \widehat{y}_i + \frac{1}{2} U_{xx} \widehat{x^2}_i + U_{xy} \widehat{xy}_i + \frac{1}{2} U_{yy} \widehat{y^2}_i = U_i - U_0, \tag{21}$$

where U_i is the cell averaged value over the neighboring triangle Ω_i, $i = 1, 2, 3$. For the nine cell interface points p_{ij}, $i, j = 1, 2, 3$, we have

$$U_x x_{ij} + U_y y_{ij} + \frac{1}{2} U_{xx} x_{ij}^2 + U_{xy} x y_{ij} + \frac{1}{2} U_{yy} y_{ij}^2 = U_{ij} - U_0, \tag{22}$$

where U_{ij} is the point-wise value of $U(x, y)$ at the point p_{ij}.

To solve the corresponding derivatives for $U(x, y)$, Eq. (21) and Eq. (22) can be written into an over-determined linear system

$$\begin{pmatrix} \widehat{x}_1 & \widehat{y}_1 & \frac{1}{2}\widehat{x^2}_1 & \widehat{xy}_1 & \frac{1}{2}\widehat{y^2}_1 \\ & & \cdots & & \\ \widehat{x}_3 & \widehat{y}_3 & \frac{1}{2}\widehat{x^2}_3 & \widehat{xy}_3 & \frac{1}{2}\widehat{y^2}_3 \\ x_{11} & y_{11} & \frac{1}{2}x_{11}^2 & xy_{11} & \frac{1}{2}y_{11}^2 \\ & & \cdots & & \\ x_{33} & y_{33} & \frac{1}{2}x_{33}^2 & xy_{33} & \frac{1}{2}y_{33}^2 \end{pmatrix} \begin{pmatrix} U_x \\ U_y \\ U_{xx} \\ U_{xy} \\ U_{yy} \end{pmatrix} = \begin{pmatrix} U_1 - U_0 \\ \cdots \\ U_3 - U_0 \\ U_{11} - U_0 \\ \cdots \\ U_{33} - U_0 \end{pmatrix}. \tag{23}$$

Denote $dU = (U_x, U_y, U_{xx}, U_{xy}, U_{yy})^T$, $\Delta U = (U_1 - U_0, \ldots, U_3 - U_0, U_{11} - U_0, \ldots, U_{33} - U_0)^T$, the above linear system is expressed as the matrix form

$$D dU = \Delta U,$$

where D is the coefficient matrix corresponding to Eq. (23).

To deal with the discontinuity, a diagonal matrix $\mathcal{W} = diag(w_1, \ldots, w_3, w_{11}, \ldots, w_{33})$ is introduced as the simple weight functions

$$w_i = \frac{1}{(s_i^2 + \epsilon)}, \qquad w_{ij} = \frac{1}{(s_{ij}^2 + \epsilon)},$$

where $s_i = \frac{U_i - U_0}{|\mathbf{x}_i - \mathbf{x}_0|}$, $s_{ij} = \frac{U_{ij} - U_0}{|\mathbf{x}_i - \mathbf{x}_0|}$, $i, j = 1, \ldots, 3$, and $\epsilon = 10^{-6}$. The derivatives dU can be obtained by solving the linear system

$$D^T \mathcal{W} D dU = D^T \mathcal{W} \Delta U.$$

Generally, for most cases with Mach number $Ma < 2$, the weighted functions are enough to deal with the discontinuity. However, for strong discontinuity, the shock detection [13] technique is used in the current scheme. Analogous to the analysis of KXRCF detector, for the third-order scheme, it is easy to distinguish the smooth region from the region near discontinuities as follows

$$U_i(\mathbf{x}_i) - U_{j \to i}(\mathbf{x}_i) = \begin{cases} O(h^3) & \text{in smooth region}, \\ O(h) & \text{near discontinuity}, \end{cases}$$

where the index i refers $\triangle_{ABC}$ and the index j refers $\triangle_{ABC'}$, $U_i(\mathbf{x}_i)$ is the interpolated value at the center of $\triangle_{ABC}$ and $U_{j \to i}(\mathbf{x}_i)$ is the value at the center of $\triangle_{ABC}$ extrapolated from $\triangle_{ABC'}$. In the computation, the "trouble cell" is detected according the following criterion

$$\max(\|U_i(\mathbf{x}_i) - U_{j \to i}(\mathbf{x}_i)\|, \|U_j(\mathbf{x}_j) - U_{i \to j}(\mathbf{x}_j)\|) \geq C \sqrt{S_{\triangle_{ABC}} + S_{\triangle_{ABC'}}} \sim O(h),$$
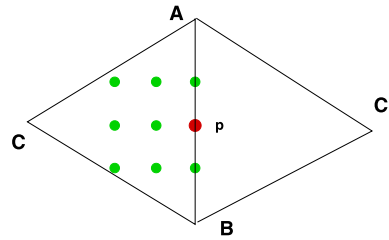
Fig. 3. The stencil of the compact reconstruction for triangle $\Omega_0 = \triangle_{ABC}$ for the characteristic variables. The coordinate of these points $p_{ij}, i, j = 1, 2, 3$ is $((i - 3)d, (j - 2)d)$, where $d = d_{AB}/4$.
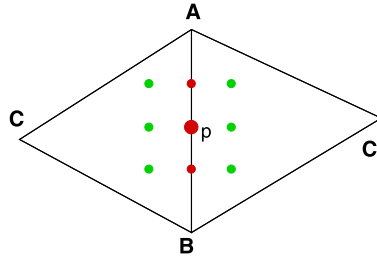

Fig. 4. The stencil for the equilibrium part in the local coordinate. The coordinate of these points $p_{ij}, i, j = 1, 2, 3$ is $((i - 2)d, (j - 2)d)$, where $d = d_{AB}/4$.

where S is the area of triangle, C is a problem dependent coefficient, and $C = 5$ is used in the computation. In those detected "trouble cell", the second order scheme with limiters are used. The above choice of weighted functions may not be optimal and further study is needed.

With the derivatives $dU = (U_x, U_y, U_{xx}, U_{xy}, U_{yy})^T$, the whole flow distribution inside the cell $\triangle_{ABC}$ in Fig. 3 can be obtained. For the smooth flow, no special treatment is needed. With $W = U$, the interpolated value W_l and the derivatives dW_l can be fully obtained in the cell $\triangle_{ABC}$. Similarly, the interpolated value W_r and the derivatives dW_r in the cell $\triangle_{ABC'}$ can be obtained with its corresponding stencil as well.

For the flow with discontinuity, the characteristic variables are reconstructed in the cell $\triangle_{ABC}$. With the derivatives $dU = (U_x, U_y, U_{xx}, U_{xy}, U_{yy})^T$, the interpolated value U at the points in Fig. 3 can be obtained. By the inverse projection, the conservative variables are obtained by $W = R_* U$, where R_* is the corresponding right eigenmatrix. Based on these point-wise values and their central differences, W_l and dW_l can be obtained. Similarly, the interpolated value W_r and the derivatives dW_r in the cell $\triangle_{ABC'}$ can be also obtained.

3.2. Reconstruction of equilibrium part

In this subsection, the reconstruction of equilibrium part will be presented. This reconstruction will be based on conservative variables W. To third-order accuracy, the Taylor expansion corresponding to equilibrium state at the center of cell interface is expressed as

$$\overline{W}(x, y) = W_0 + \overline{W}_x(x - x_p) + \overline{W}_y(y - y_p) + \frac{1}{2}\overline{W}_{xx}(-x_p)^2 + \overline{W}_{xy}(x - x_p)(y - y_p) + \frac{1}{2}\overline{W}_{yy}(y - y_p)^2, \quad (24)$$

where W_0 is the conservative variable at the center of cell interface AB based on the compatibility condition Eq. (14), and $\overline{W}_x, \ldots, \overline{W}_{yy}$ are corresponding derivatives.

As shown in Fig. 4, with the reconstructed polynomials in $\triangle_{ABC}$ and $\triangle_{ABC'}$, the point values at those points can be determined, which have been obtained in the last subsection. Especially, we can get the point values at the interface (red) points at both sides of AB. By the compatibility condition Eq. (2), the reconstructed conservative variables at the cell interface can be determined. The derivatives $\overline{W}_x, \ldots, \overline{W}_{yy}$ can be obtained by the central differences of these point-wise values.

3.2.1. Extension to rectangular meshes

For the rectangular mesh, the stencil used is given in Fig. 5. To reconstruct the polynomial for the rectangle $\square_{ABCD}$, the cell averaged values $U_i, i = 1, 2, 3, 4$ and point-wise values $p_{ij}, i, j = 1, 2, 3, 4$ at the cell interfaces can be used. Similar to the triangular case, we have the following matrix form for the over-determined linear system

$$D_2 dU = \Delta U,$$

where $dU = (U_x, U_y, U_{xx}, U_{xy}, U_{yy})^T$, $\Delta U = (U_1 - U_0, \ldots, U_4 - U_0, U_{11} - U_0, \ldots, U_{44} - U_0)^T$. D_2 is the coefficient matrix and expressed as
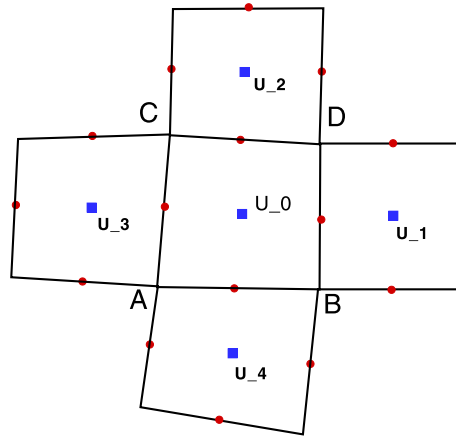
Fig. 5. The stencil for the rectangular mesh. The red circles represent the point-wise values and the blue squares are the cell averaged values. (For interpretation of the references to color in this figure legend, the reader is referred to the web version of this article.)

$$
D_2 = \begin{pmatrix} \widehat{x}_1 & \widehat{y}_1 & \frac{1}{2}\widehat{x^2}_1 & \widehat{xy}_1 & \frac{1}{2}\widehat{y^2}_1 \\ & & \cdots & & \\ \widehat{x}_4 & \widehat{y}_4 & \frac{1}{2}\widehat{x^2}_4 & \widehat{xy}_4 & \frac{1}{2}\widehat{y^2}_4 \\ x_{11} & y_{11} & \frac{1}{2}x_{11}^2 & xy_{11} & \frac{1}{2}y_{11}^2 \\ & & \cdots & & \\ x_{14} & y_{44} & \frac{1}{2}x_{44}^2 & xy_{44} & \frac{1}{2}y_{44}^2 \end{pmatrix}.
$$

By introducing the weight diagonal matrix $\mathcal{W}_2 = diag(w_1, \ldots, w_4, w_{11}, \ldots, w_{44})$, the derivatives dU can be also obtained by solving the following linear system

$$
D_2^T \mathcal{W}_2 D_2 dU = D_2^T \mathcal{W}_2 \Delta U.
$$

The limiting process is also needed for the flow with large discontinuity. The reconstruction for equilibrium part can be extended to the rectangular meshes directly.

Similarly, it is straightforward to extend the compact reconstruction to any hybrid three-dimensional meshes. To the third-order accuracy, the macroscopic variables $U = U(x, y, z)$ need to be expanded in the three-dimensional space. The whole polynomial can be fully determined by the weighted least square method for any three-dimensional meshes with a compact stencil. The scheme for the three-dimensional flows will be developed in the future.

4. Numerical tests

In this section, numerical tests for both inviscid and viscous flow will be presented to validate the compact scheme. For the inviscid flow, the collision time τ takes

$$
\tau = \epsilon \Delta t + c |\frac{p_l - p_r}{p_l + p_r}| \Delta t,
$$

where $\varepsilon = 0.05$. For the viscous flow, we use

$$
\tau = \frac{\mu}{p} + c |\frac{p_l - p_r}{p_l + p_r}| \Delta t,
$$

where p_l and p_r denote the pressure on the left and right sides of the cell interface, μ is the viscous coefficient, p is the pressure at the cell interface, and $c = 1$. In the smooth flow regions, it will reduce to $\tau = \mu/p$. The ratio of specific heats takes $\gamma = 1.4$. Δt is the time step which is determined according to the CFL condition.

The ghost cell method is used to deal with boundary condition. The ghost elements are reflected according to the local coordinate of boundary cell interface. The macroscopic variables inside these elements are imposed according to the specific boundary conditions.

Before the numerical tests are presented, the computational costs for the compact third-order scheme with both structured and unstructured meshes are tested by the one-dimensional Riemann problem in a domain $[0, 1] \times [0, 1]$. The characteristic variables are used in the spatial reconstruction. As a reference, the CPU times for different schemes are tested by 10 time steps with Intel Core i7-4770 CPU @ 3.40 GHz. The compact schemes based on the rectangular mesh and the triangular mesh are all tested with the mesh size $h = 1/100$. The total number of cell interface, the total number of the

Table 1

The computational cost for the compact-GKS and WENO-GKS with characteristic reconstruction.

Scheme	No. of element	No. of interface	Time
Triangular compact-GKS	23208	34406	10.34127 s
Rectangular compact-GKS	10000	20200	6.45086 s
Structured WENO-GKS	10000	20200	1.38178 s

Table 2

Accuracy test for the isotropic vortex problem.

Mesh	L^∞ norm	Order
1/30	3.2460690E–03	
1/50	7.3230267E–04	2.914901
1/100	9.2029572E–05	2.992271
1/200	1.1801720E–05	2.963100
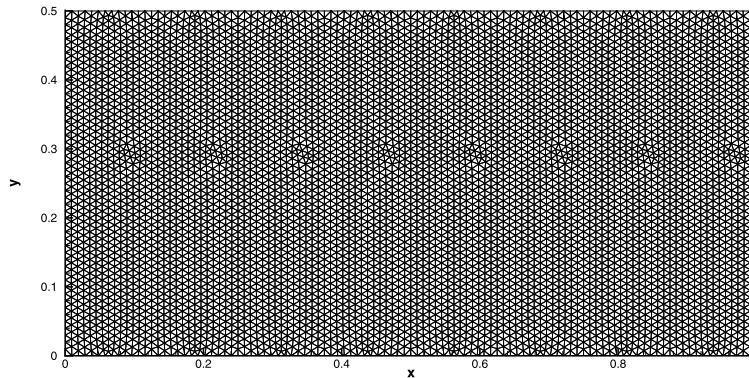
Fig. 6. 1D Riemann problem: the high-quality mesh for the 1D Riemann problem.

rectangular, and triangular meshes, and the computational time are all presented in Table 1. More number of cell interface introduce more computational cost. Its computational cost for the WENO gas-kinetic scheme based on the structured mesh is also given in Table 1. The uniform mesh with $\Delta x = \Delta y = 1/100$ is used. The computational cost is also presented in Table 1. Compared with the WENO-GKS, the compact scheme costs much more computational time. The main reasons are given as follows. Different from the reconstruction on structured meshes, more time is spent on searching the elements for reconstruction on unstructured meshes. The coefficients are identical for different elements on the uniform mesh for the WENO reconstruction. However, the weighted least square procedure needs to be done for different elements on unstructured meshes, and the matrix computing costs much more time for different elements. The characteristic projection procedure is another source that costs much computational time. In the current scheme, the initial reconstruction is done for each cell interface in the local coordinate. Thus, for each cell, the initial reconstruction is conducted repeatedly. When taking the initial reconstruction in a global coordinate and doing the reconstruction for each cell once at each time step, the computational cost can be much reduced.

4.1. Accuracy test

The numerical order of the compact gas-kinetic scheme is tested in comparison with the analytical solutions of the Euler equations. The isotropic vortex propagation problem is presented to validate the accuracy for the solution of inviscid flow. The computational domain is taken to be $[0, 1.5] \times [0, 1.5]$. The free upstream is $(\rho, u, v, p) = (1.21, 0, 0, 1)$, and a small vortex is obtained through a perturbation on the mean flow with the velocity (u, v), temperature $T = p/\rho$, and entropy $S = \ln(p/\rho^\gamma)$. The perturbation is expressed as

$$(\delta u, \delta v) = \kappa \eta e^{\mu(1-\eta^2)}(\sin\theta, -\cos\theta),$$

$$\delta T = -\frac{(\gamma - 1)\kappa^2}{4\mu\gamma}e^{2\mu(1-\eta^2)}, \delta S = 0,$$

where $\eta = r/r_c$, $r = \sqrt{(x - x_c)^2 + (y - y_c)^2}$, $(x_c, y_c) = (0.75, 0.75)$, $\kappa = 0.3$, $\mu = 0.204$, and $r_c = 0.05$. In the computation, the unstructured meshes with mesh size $h = 1/30, 1/50, 1/100$ and $1/200$ are used, and the L^∞ errors and orders at $t = 1$ are presented in Table 2, which shows a third-order accuracy for the current compact scheme.
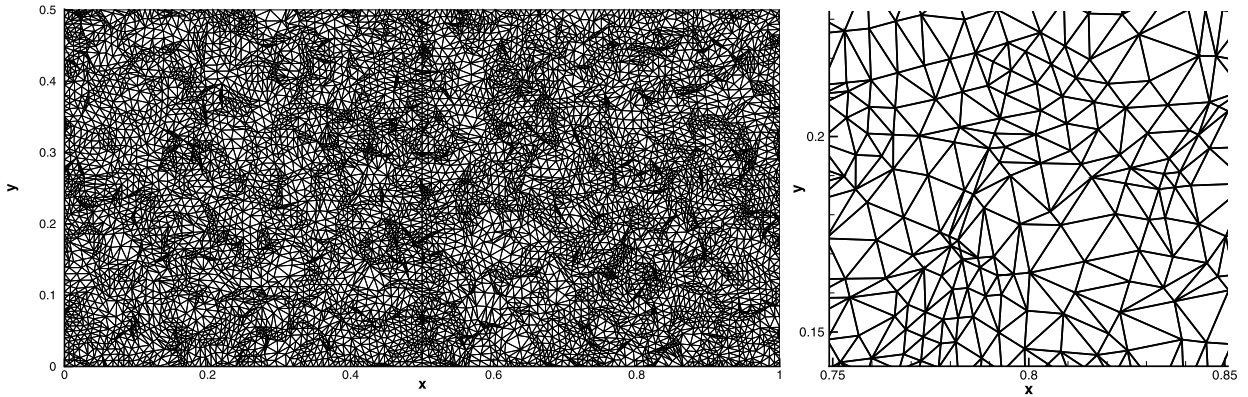
Fig. 7. 1D Riemann problem: the low-quality mesh and local enlargement for the 1D Riemann problem.
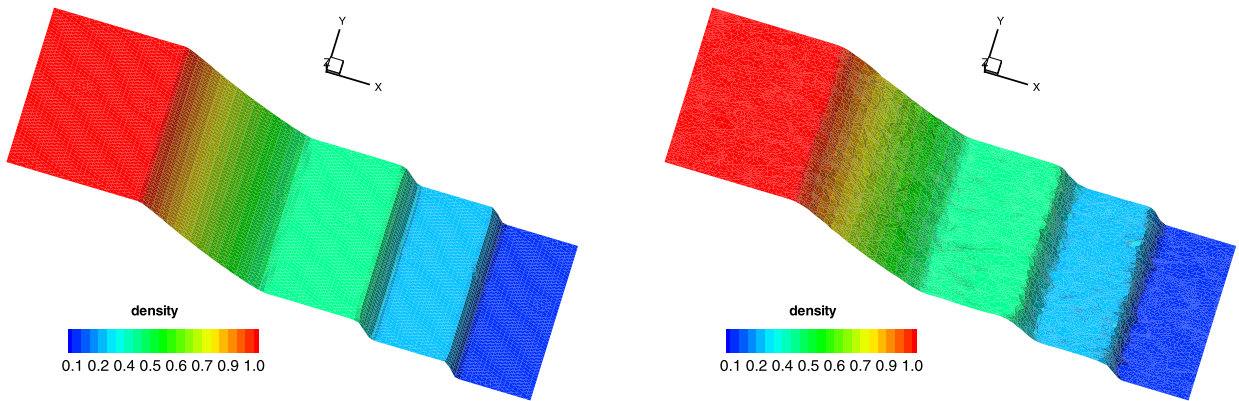

Fig. 8. 1D Riemann problem: the density distribution for the Sod problem with the high-quality (left) and low-quality (right) meshes in the whole computational domain.

4.2. One dimensional Riemann problem

In this case, two one-dimensional Riemann problems are tested to verify the capability in capturing the wave configurations. The mesh is presented in Fig. 6, where the computational domain is $[0, 1] \times [0, 0.5]$, and mesh size is $h = 0.01$.

4.2.1. Sod problem
The initial condition for this problem is given by

$$(\rho, u, p) = \begin{cases} (1, 0, 1), 0 < x < 0.5, \\ (0.125, 0, 0.1), 0.5 < x < 1. \end{cases}$$

In this case, the weighted least square reconstruction can deal with the discontinuity well, and the shock detection technique is not needed. The density distributions are given in Fig. 8 in the whole computational domain at $t = 0.2$. The density, velocity, and pressure distributions for the numerical results and the exact solutions are presented in Fig. 9. The numerical results agree well with the exact solutions.

The stability for the current scheme is tested by the Sod problem. The velocity profiles with different *CFL* numbers from 0.3 to 0.7, are shown in Fig. 10. The scheme is basically stable under the conventional CFL condition. The waves profiles can be well resolved at a *CFL* number around 0.5. The value of 0.35 is already more than two times of the time step used for the compact third-order DG method. In the following numerical tests, without spacial statement, the *CFL* number takes a fixed value of 0.35.

For the mesh with highly stretched elements, which are shown in Fig. 7, the Sod problem is also tested to show the robustness and performance of compact scheme with *CFL* = 0.35. The density distribution in the whole computational domain is given in Fig. 8. Due to the low-quality mesh, the shock detection technique is needed and a stable solution can be obtained. However, the obvious fluctuation can be observed as well.
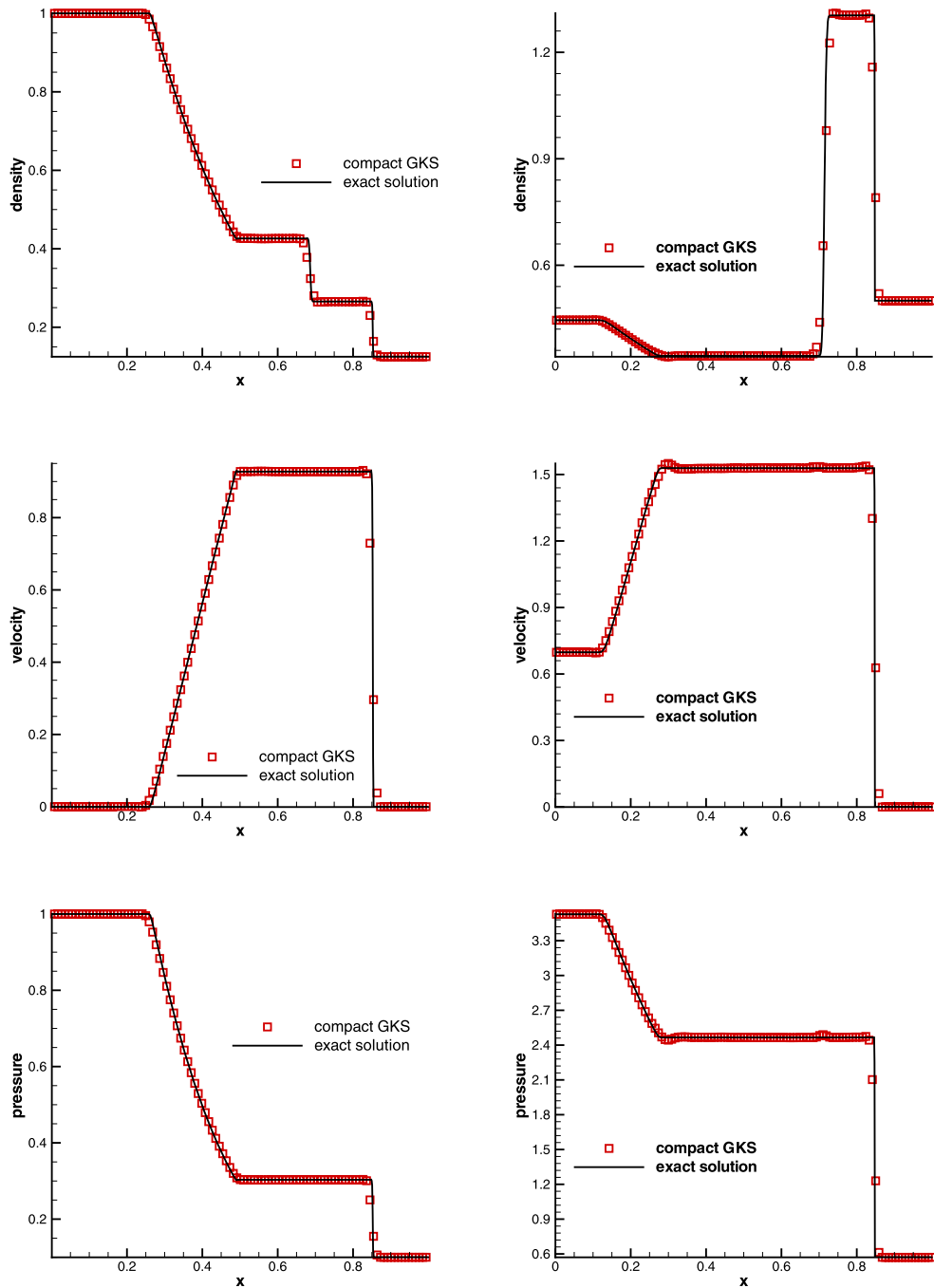
Fig. 9. 1D Riemann problem: Sod problem (left): the density, velocity, and pressure distributions at $t = 0.2$, and Lax problem (right): the density, velocity, and pressure distributions at $t = 0.14$, where the mesh size is $h = 1/100$.

4.2.2. Lax problem

The initial condition for this problem is given as follows

$$(\rho, u, p) = \begin{cases} (0.445, 0.698, 3.528), & 0 \leq x < 0.5, \\ (0.5, 0, 0.571), & 0.5 \leq x \leq 1. \end{cases}$$

The shock detection technique is not needed. The density, velocity, and pressure distributions for the numerical results and the exact solutions are presented in Fig. 9 at $t = 0.14$. The numerical results agree well with the exact solutions.
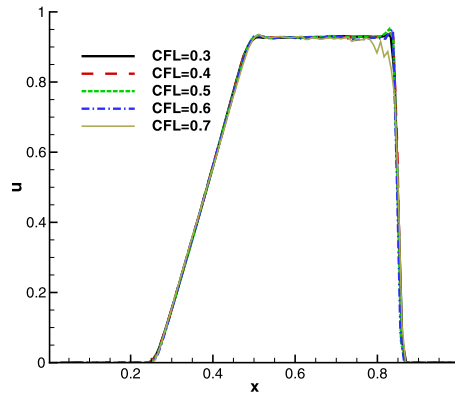
Fig. 10. The stability test for the Sod problem.
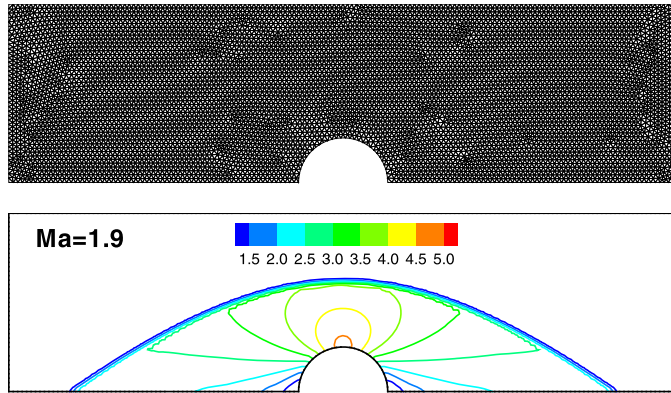
Fig. 11. Flow impinging on a blunt body: the mesh and pressure distribution at $Ma = 1.9$.

4.3. Flow impinging on a blunt body

In this case, the inviscid hypersonic flow impinging on a unit cylinder is tested to validate robustness of the current scheme. This problem is initialized by the flow moving towards a cylinder with different Mach numbers. The Euler boundary condition is imposed on the surface of cylinder, and outflow boundary condition on the right boundary. As mentioned in the reconstruction part, the weighted least square reconstruction is able to deal with the discontinuities at a Mach number $Ma < 2$. In this case, the flow with $Ma = 1.9$ is tested without the detection of "trouble cell". The mesh and the pressure distribution for this case are given in Fig. 11. With mesh size $h = 1/15$, the flow structure can be captured nicely in front of the cylinder. However, with a high Mach number, the weighted least square reconstruction is no longer able to capture strong discontinuities, and the shock detection technique is used to identify the trouble cells, where a second-order reconstruction is used in these cells. For the flow with $Ma = 8$, the mesh and the pressure distribution are shown in Fig. 12 with mesh size $h = 1/15$. This test shows that the current scheme can capture the flow structure nicely in front of the cylinder and the carbuncle phenomenon does not appear [22].

4.4. Shock vortex interaction

The interaction between a stationary shock and a vortex for the inviscid flow is presented [11]. The computational domain is taken to be $[0, 1.5] \times [0, 1]$. A stationary Mach 1.1 shock is positioned at $x = 0.5$ and normal to the x-axis. The left upstream state is $(\rho, u, v, p) = (Ma^2, \sqrt{\gamma}, 0, 1)$, where Ma is the Mach number. A small vortex is obtained through a perturbation on the mean flow with the velocity (u, v), temperature $T = p/\rho$, entropy $S = \ln(p/\rho^\gamma)$, the perturbation is expressed as

$$(\delta u, \delta v) = \kappa \eta e^{\mu(1-\eta^2)}(\sin\theta, -\cos\theta),$$

$$\delta T = -\frac{(\gamma - 1)\kappa^2}{4\mu\gamma} e^{2\mu(1-\eta^2)}, \delta S = 0,$$

where $\eta = r/r_c$, $r = \sqrt{(x - x_c)^2 + (y - y_c)^2}$ with $(x_c, y_c) = (0.25, 0.5)$ as the center of the vortex. Here κ indicates the strength of the vortex, μ controls the decay rate of the vortex, and r_c is the critical radius for which the vortex has the
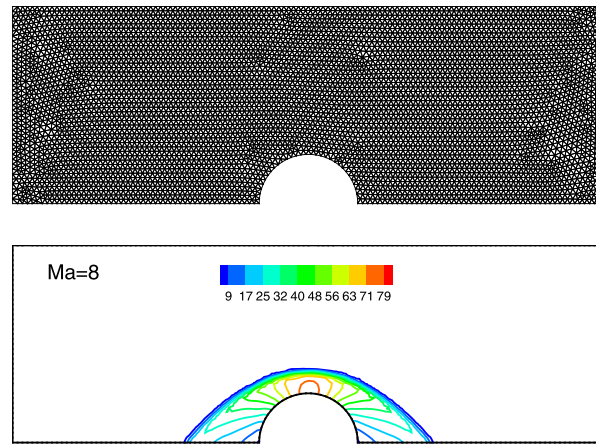
Fig. 12. Flow impinging on a blunt body: the mesh and pressure distribution at $Ma = 8$.
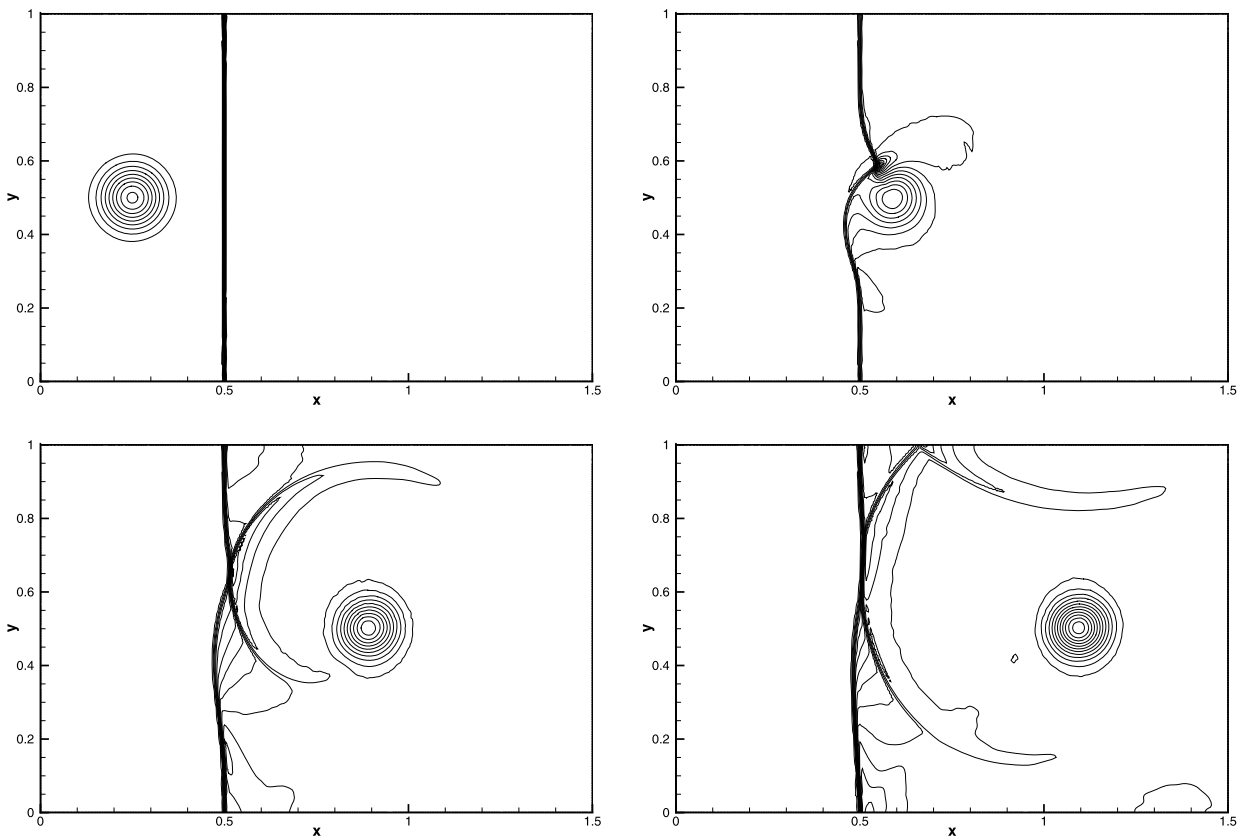

Fig. 13. Shock vortex interaction: the pressure distributions at $t = 0.3$ and 0.8 with mesh size $h = 1/150$.

maximum strength. In the computation, $\kappa = 0.3$, $\mu = 0.204$, and $r_c = 0.05$. The reflected boundary conditions are used on the top and bottom boundaries. The pressure distributions with mesh size $h = 1/150$ at $t = 0, 0.3, 0.6$ and 0.8 are shown in Fig. 13. The detailed pressure distribution along the center horizontal line with mesh size $h = 1/50, 1/100$, and $1/150$ at $t = 0.8$ are shown in Fig. 14. This case is tested without the detection of "trouble cell", which shows the robustness of the weighted least square reconstruction to deal with the flow with weak discontinuities. Based on the weighted least square method, the third-order scheme can be extended to the non-compact stencil directly, which is shown in Fig. 1. The non-compact scheme is also tested by this case. The pressure distribution along the center horizontal line for the compact and non-compact scheme with mesh size $h = 1/50$ at $t = 0.8$ are shown in Fig. 15. The performance of two schemes are nearly identical.
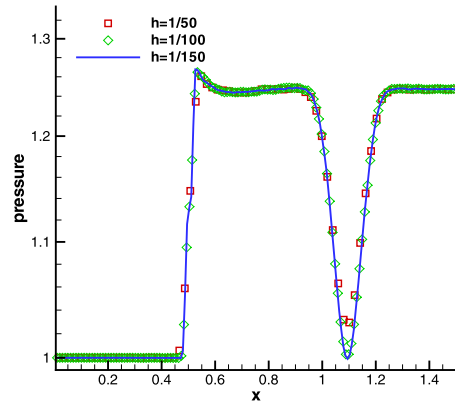
Fig. 14. Shock vortex interaction: the pressure distribution at $t = 0.8$ along the horizontal symmetric line $y = 0.5$ with mesh size $h = 1/50, 1/100$ and $1/150$.
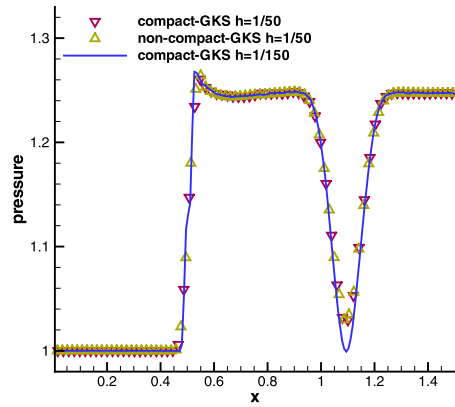

Fig. 15. Shock vortex interaction: the pressure distribution at $t = 0.8$ along the horizontal symmetric line for the compact and non-compact schemes with a mesh size $h = 1/50$.
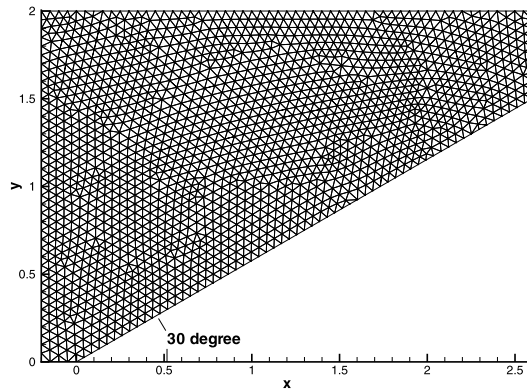

Fig. 16. Double Mach reflection: computational domain with mesh size $h = 1/20$.

4.5. Double Mach reflection problem

This problem was extensively studied by Woodward and Colella for the inviscid flow [24]. A shock moves down in a tube which contains a 30° wedge. The computational domain is shown in Fig. 16 with mesh size $h = 1/20$. The shock wave has a strength with Mach number 10, which is initially positioned at $x = 0$. The initial pre-shock and post-shock conditions are

$$(\rho, u, v, p) = (8, 8.25, 0, 116.5),$$
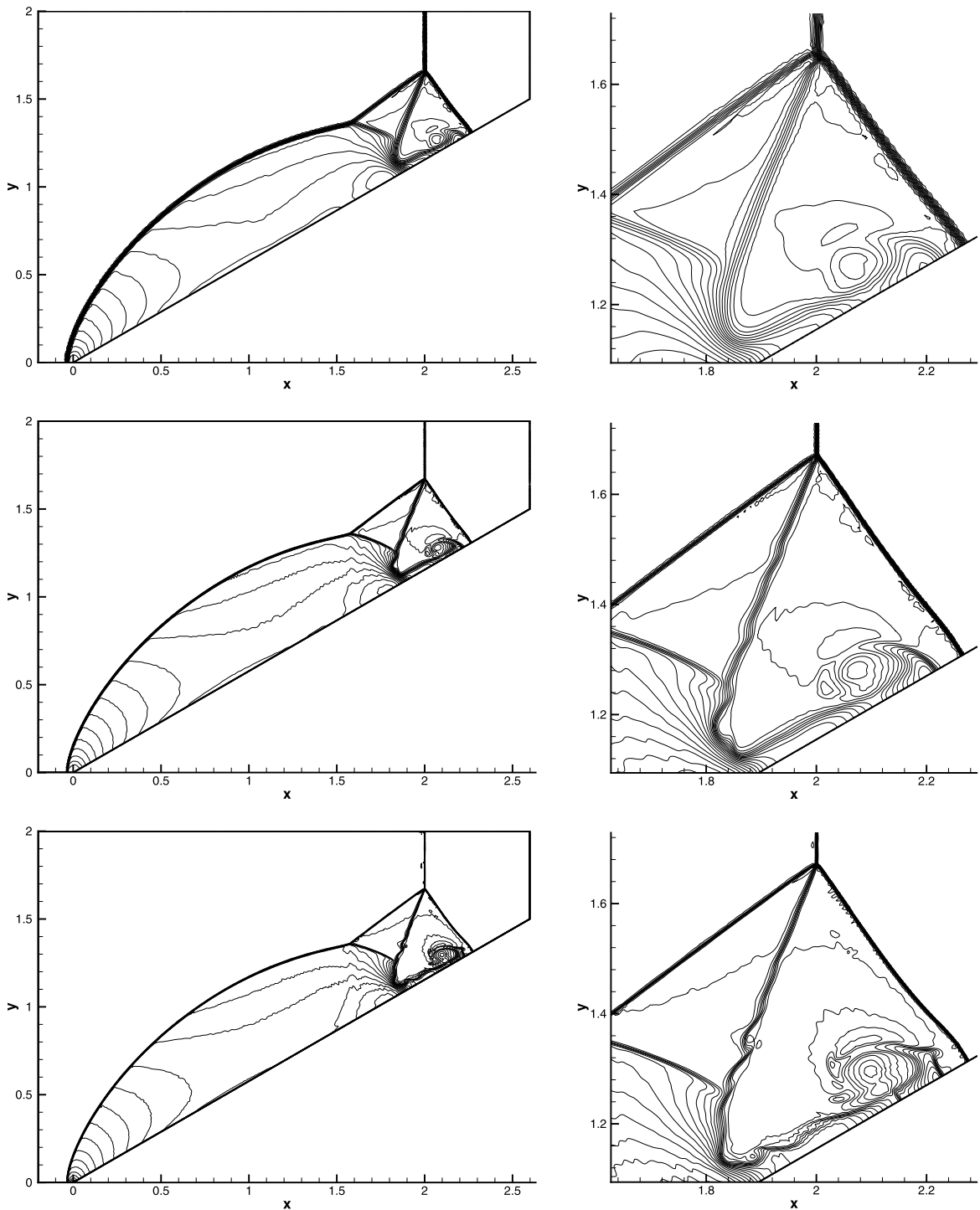$$(\rho, u, v, p) = (1.4, 0, 0, 1).$$

Fig. 17. Double Mach reflection: density contours with the mesh size $h = 1/120, 1/240,$ and $1/360$.

The reflective boundary conditions are used along the wedge, while for the rest of bottom boundary, the exact post-shock condition is imposed. At the top boundary, the flow variables are set to describe the exact motion of the shock front along the wall. The inflow and outflow boundary conditions are used at the entrance and the exit. In this case, the weighted least square reconstruction is not enough, and the shock detection technique is used to switch to the second-order initial reconstruction. The density distributions with mesh size $h = 1/120, 1/240$ and $1/360$ at $t = 0.2$ are shown in Fig. 17. The compact scheme resolves the flow structure under the triple Mach stem clearly.
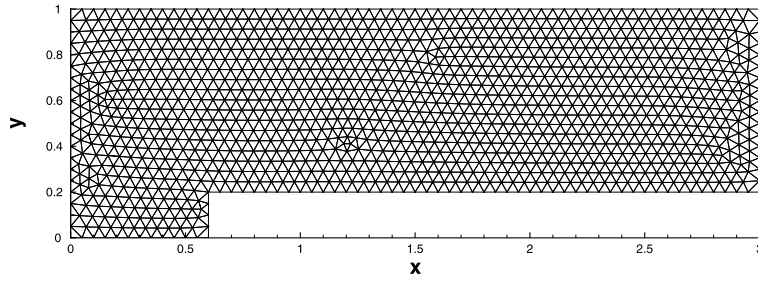
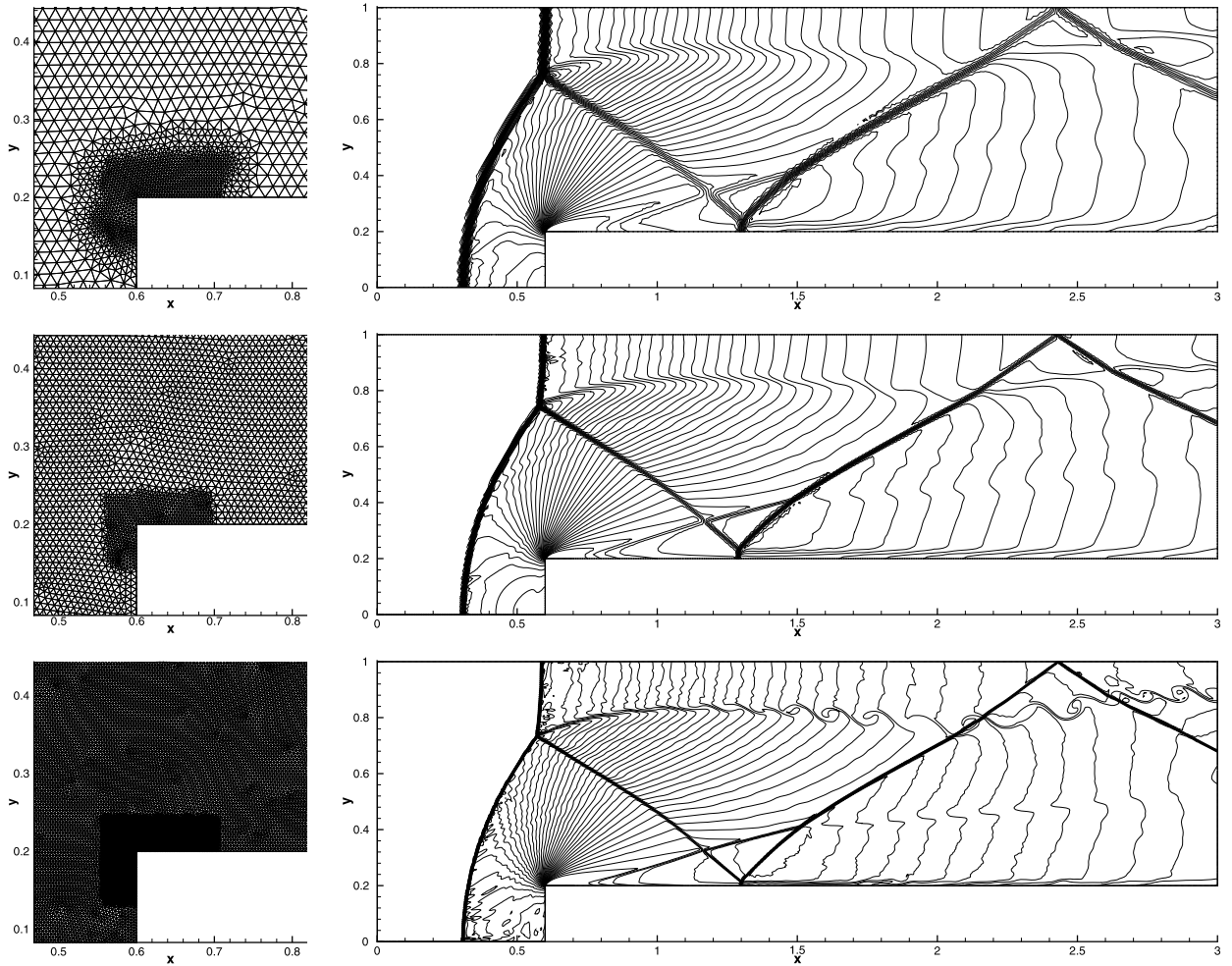**Fig. 18.** Mach step problem: the computational domain with mesh size $h = 1/20$.

Fig. 19. Mach step problem: density contours with the mesh size $h = 1/60, 1/120$, and $1/240$.

4.6. Mach step problem

The Mach step problem was again studied extensively by Woodward and Colella [24] for the inviscid flow. The computational domain $[0, 3] \times [0, 1]$ is shown in Fig. 18, which is covered by unstructured mesh with mesh size $h = 1/20$. The Mach step is located at $x = 0.6$ with height 0.2 in the tunnel. Initially, a right-moving flow with Mach 3 is imposed in the whole computational domain. The reflective boundary conditions are used along the walls of the tunnel, and inflow and outflow boundary conditions are used at the entrance and the exit. The corner of the step is the center of a rarefaction fan, which is a singular point. To minimize the numerical error generated at the corner, the meshes near the corner are refined, as shown in Fig. 19. In this case, the weighted least square reconstruction is not enough, and the shock detection technique is used again to switch to the second-order reconstruction. The density distributions with $h = 1/60, 1/120$, and $1/240$ at $t = 4$
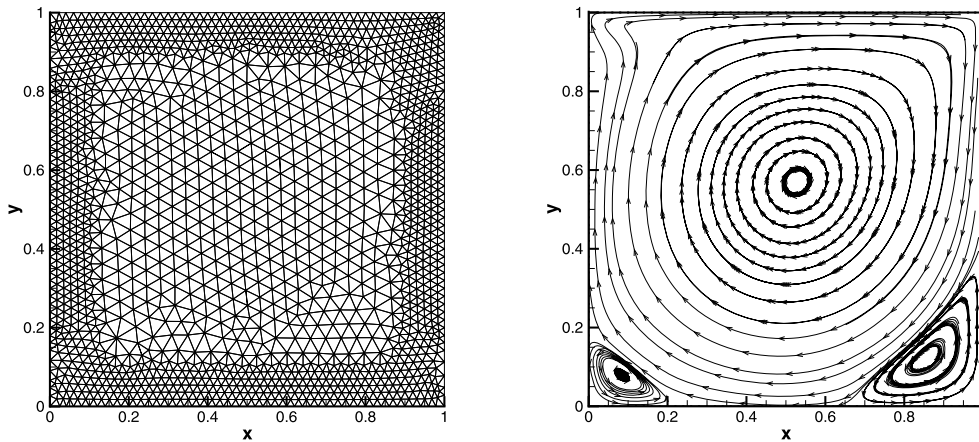
Fig. 20. Lid-driven cavity flow: mesh and streamlines for the compact gas-kinetic scheme with $Re = 1000$.

are presented in Fig. 19. With the mesh refinement, the resolution is improved, especially for the slip line started from the triple point.

4.7. Lid-driven cavity flow

The lid-driven cavity problem is one of the most important benchmarks for validating incompressible or low speed Navier–Stokes flow solvers. The fluid is bounded by a unit square and driven by a uniform translation of the top boundary. In this case, the gas has a specific heat ratio $\gamma = 5/3$ and the up wall is moving with a speed of Mach number $Ma = 0.15$. Isothermal and nonslip boundary conditions are imposed. The computational domain $[0, 1] \times [0, 1]$ with unstructured mesh is presented in Fig. 20, where mesh sizes are $h = 1/25$ for the inner cells and $h = 1/50$ near the walls. Numerical simulations are conducted for three Reynolds numbers $Re = 400, 1000$ and 3200. The streamlines with $Re = 1000$ for the compact scheme are shown in Fig. 20. The results of U-velocities along the center vertical line, V-velocities along the center horizontal line, and the benchmark data [8] are shown in Fig. 21 for $Re = 400, 1000, 3200$. The simulation results match well with the benchmark data.

4.8. Laminar boundary layer

A laminar boundary layer is tested over a flat plate with length $L = 100$. The Mach number of the free-stream is $Ma = 0.15$ and the Reynolds number is $Re = U_\infty L/\nu = 10^5$, ν is the viscous coefficient. This case is tested with the compact schemes for both triangular and rectangular meshes. Fig. 22 presents both triangular and rectangular meshes, with an enlarged view of meshes near the boundary. The non-slip adiabatic boundary condition at the plate is used and a symmetry condition is imposed at the bottom boundary before the flat plate. The non-reflecting boundary condition based on the Riemann invariants is adopted for the other boundaries. The non-dimensional velocity U and V at different locations are given in Fig. 23 for the triangular mesh, and in Fig. 24 for the rectangular mesh. In all locations, the numerical solutions match with the exact Blasius solutions very well. Here the boundary layer can be resolved by six or seven mesh points. The solutions show good performance of the compact scheme for the Navier–Stokes solutions with unstructured meshes.

4.9. Viscous shock tube problem

This problem was introduced in [5] to test the performances of different schemes for viscous flows. In this case, an ideal gas is at rest in a two-dimensional unit box $[0, 1] \times [0, 1]$. A membrane located at $x = 0.5$ separates two different states of the gas and the dimensionless initial states are

$$(\rho, u, p) = \begin{cases} (120, 0, 120/\gamma), \, 0 < x < 0.5, \\ (1.2, 0, 1.2/\gamma), \, 0.5 < x < 1, \end{cases}$$

where $Re = 200$ and Prandtl number $Pr = 0.73$.

The membrane is removed at time zero and wave interaction occurs. A shock wave, followed by a contact discontinuity, moves to the right with a Mach number $Ma = 2.37$, and reflects at the right end wall. After the reflection, it interacts with the contact discontinuity. The contact discontinuity and shock wave also interact with the horizontal wall and create a thin boundary layer during their propagation. The solution will develop complex two-dimensional shock/shear/boundary-layer interactions. This case is tested in the computational domain $[0, 1] \times [0, 0.5]$. A symmetrical condition is used on the
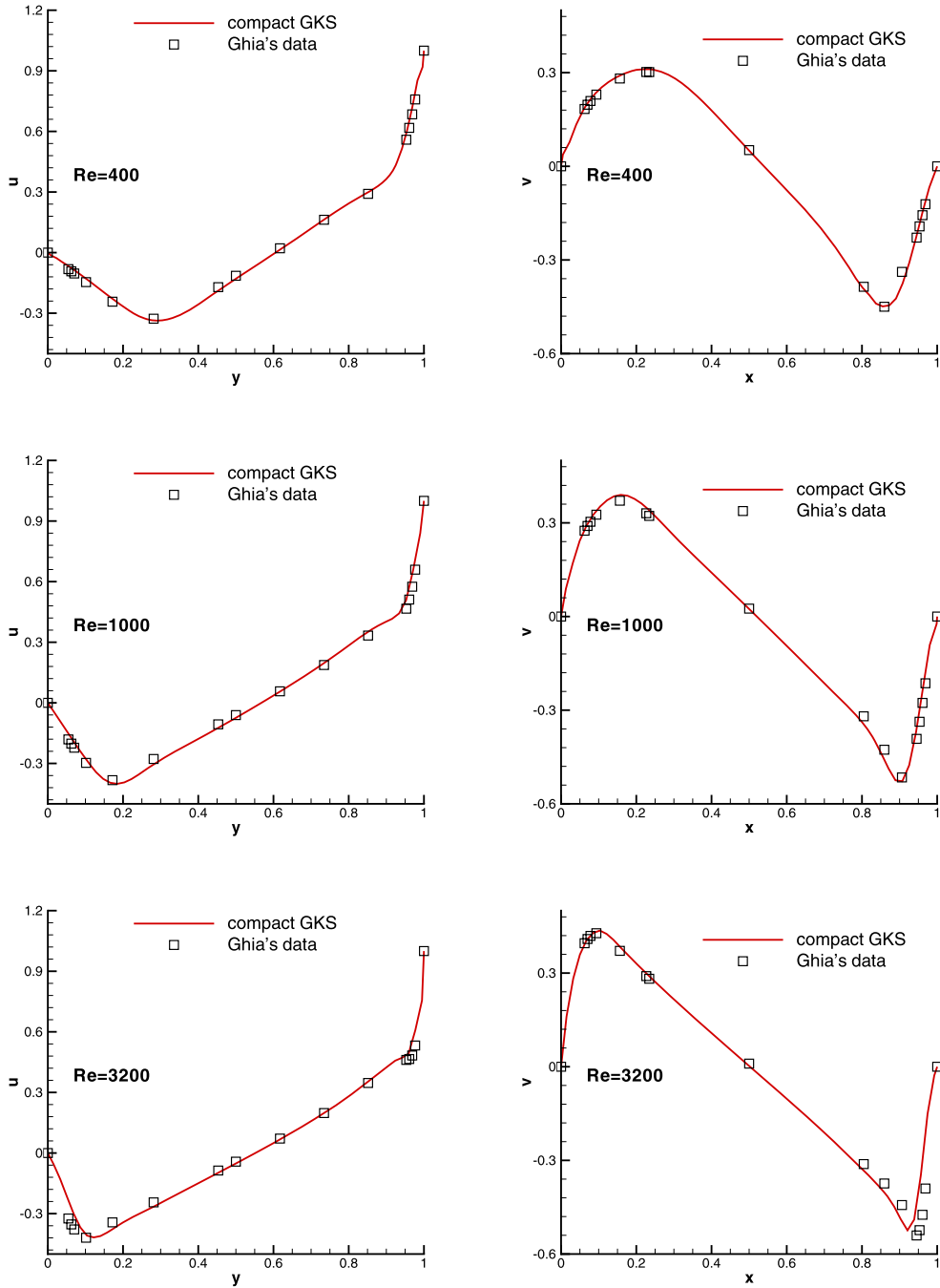
Fig. 21. Lid-driven cavity flow: U-velocities along vertical centerline line and V-velocities along horizontal centerline with $Re = 400, 1000$ and 3200. The reference data is from Ghia [8].

Table 3
Comparison of the height of primary vortex between gas-kinetic schemes and reference data [12] for the reflected shock-boundary layer interaction.

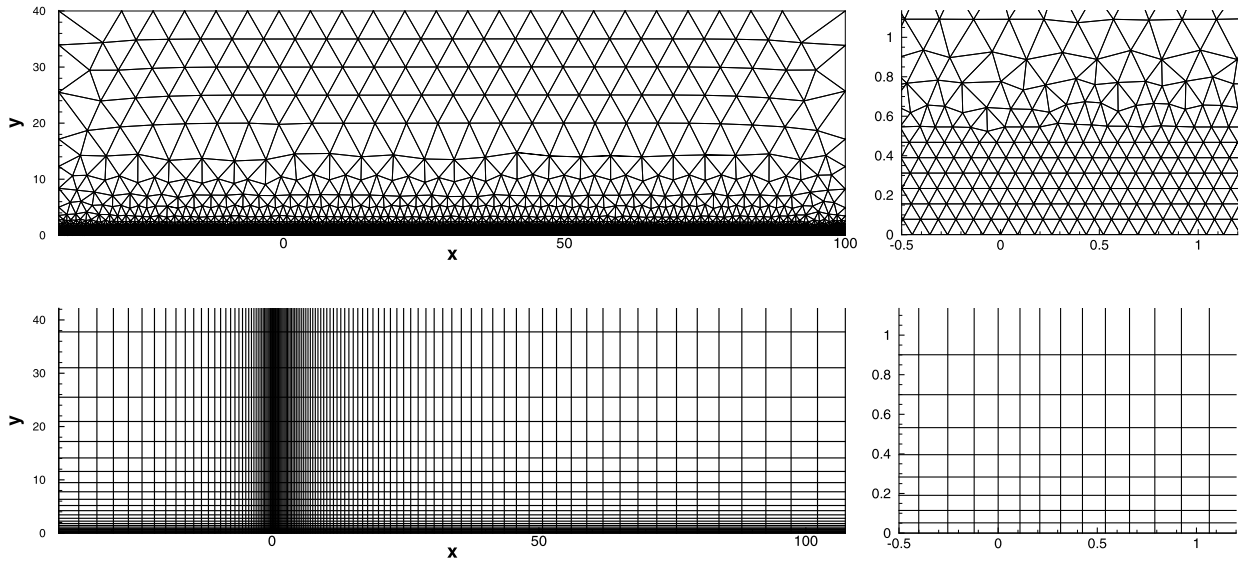| Scheme	AUSMPW+	M-AUSMPW+	WENO-GKS structured	Compact-GKS triangular	Compact-GKS rectangular
Height	0.163	0.168	0.165	0.164	0.166

Fig. 22. Laminar boundary layer computation: the triangular and rectangular meshes.
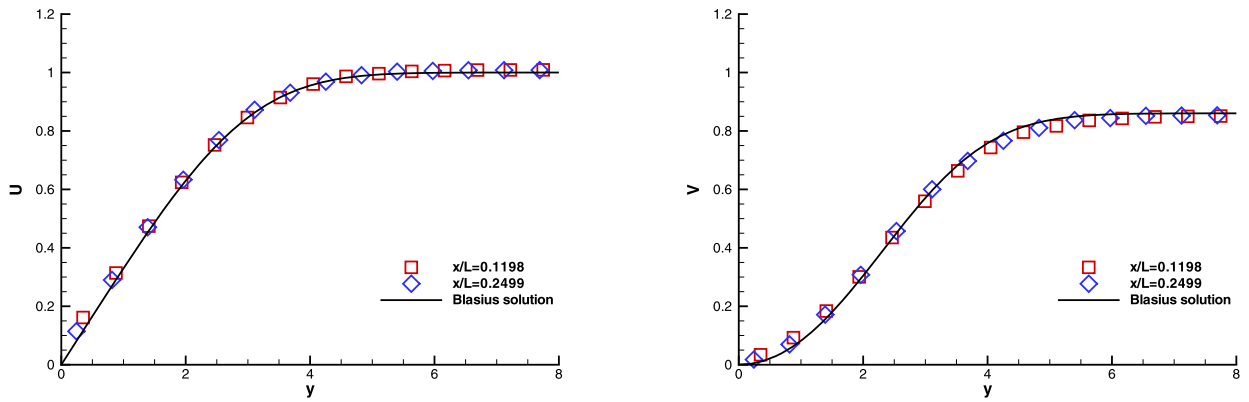

Fig. 23. Laminar boundary layer solution from compact scheme with triangular mesh: the non-dimensional velocity U and V.
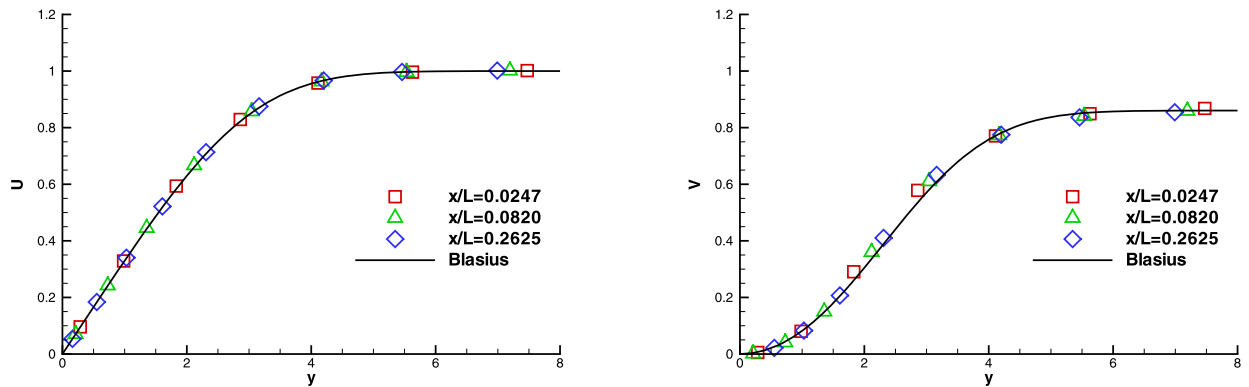

Fig. 24. Laminar boundary layer solution from compact scheme with rectangular mesh: the non-dimensional velocity U and V.
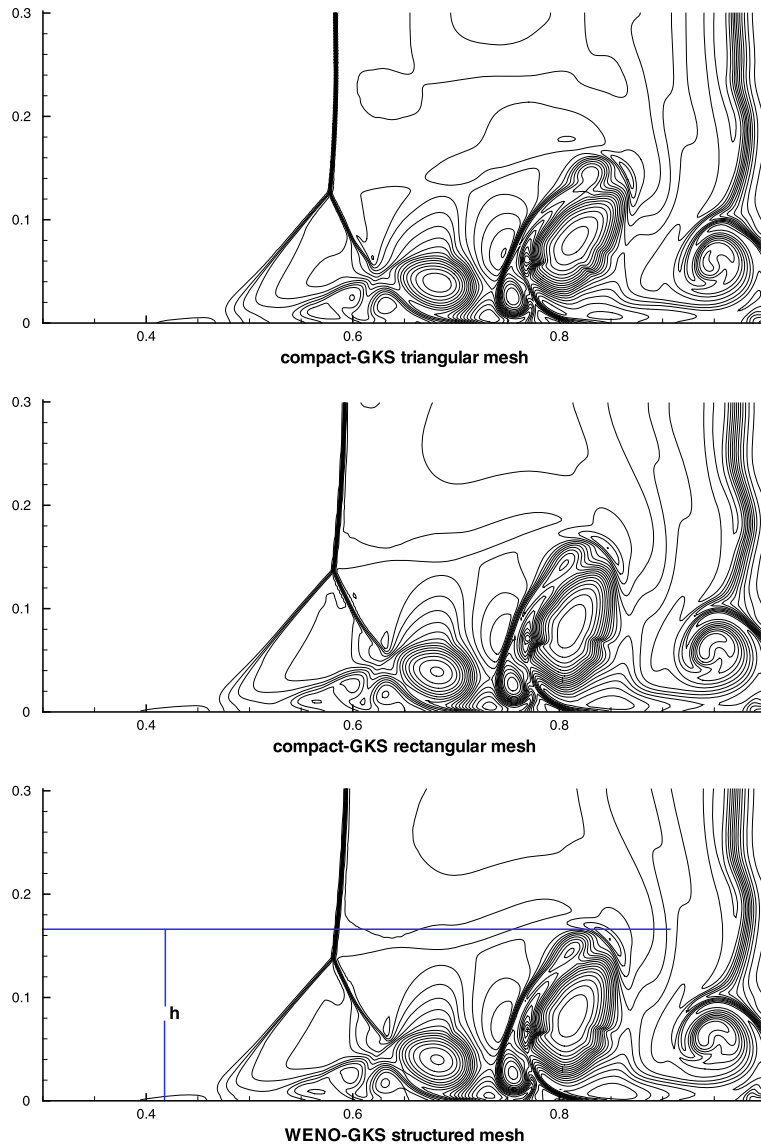
Fig. 25. Reflected shock-boundary layer interaction: the density distribution at $t = 1$ with $Re = 200$.

top boundary $x \in [0, 1]$, $y = 0.5$, and non-slip boundary condition for velocity and adiabatic condition for temperature are imposed at solid wall boundaries. The density distributions from the compact scheme with the rectangular mesh and the triangular mesh with mesh size $h = 1/500$ are given in Fig. 25. As a reference, the density distribution of the third-order WENO-GKS with a structured mesh size $\Delta x = \Delta y = 1/500$ is also presented [17]. The current scheme can resolve the complex flow structure. As shown in Table 3, the height of primary vortex predicted by the current scheme agrees well with the reference data [12] and the third-order WENO-GKS results on the structured mesh.

5. Conclusion

In this paper, a third-order compact gas-kinetic scheme is proposed on unstructured meshes for both inviscid and viscous flow simulations. The novelty of gas-kinetic scheme is that the time-dependent gas distribution function at cell interface can provide both numerical fluxes and the point-wise flow variables at next time level due to its high-order gas evolution model. Therefore, the scheme can be designed in a compact way, where both the cell averaged and cell interface flow variables can be used for the initial data reconstruction at the beginning of next time level. With the inclusion of neighboring cells only, a compact third-order gas-kinetic scheme is constructed, where the weighted least-square technique is used for the data reconstruction on the unstructured meshes. In comparison with former compact gas-kinetic scheme, the use of least-square procedure avoids the difficulty in choosing different stencils. The systematic way of including all weighted stencils makes

the compact reconstruction suitable for different kinds of meshes. Different from other higher-order schemes based on the Riemann solution, the current method avoids the use of Gaussian points integration for the flux transport along a cell interface and the multi-stage Runge–Kutta time stepping technique. The compact scheme has been tested in both smooth viscous flow and the flows with strong discontinuities. The numerical results confirm the accuracy and robustness of the third-order compact gas-kinetic scheme.

Acknowledgements

References

[1] R. Abgrall, On essentially non-oscillatory schemes on unstructured meshes: analysis and implementation, J. Comput. Phys. 144 (1994) 45–58.
[2] T.J. Barth, P.O. Frederichson, Higher order solution of the Euler equations on unstructured grids using quadratic reconstruction, AIAA 90-0013, 1990.
[3] P.L. Bhatnagar, E.P. Gross, M. Krook, A model for collision processes in gases I: small amplitude processes in charged and neutral one-component systems, Phys. Rev. 94 (1954) 511–525.
[4] S. Chapman, T.G. Cowling, The Mathematical Theory of Non-Uniform Gases, third edition, Cambridge University Press, 1990.
[5] V. Daru, C. Tenaud, High order one-step monotonicity-preserving schemes for unsteady compressible flow calculations, J. Comput. Phys. 193 (2004) 563–594.
[6] M. Dumbser, M. Käser, V.A. Titarev, E.F. Toro, Quadrature-free non-oscillatory finite volume schemes on unstructured meshes for nonlinear hyperbolic systems, J. Comput. Phys. 226 (2007) 204–243.
[7] O. Friedrich, Weighted essentially non-oscillatory schemes for the interpolation of mean values on unstructured grids, J. Comput. Phys. 144 (1998) 194–212.
[8] U. Ghia, K.N. Ghia, C.T. Shin, High-Re solutions for incompressible flow using the Navier–Stokes equations and a multigrid method, J. Comput. Phys. 48 (1982) 387–411.
[9] Z.L. Guo, K. Xu, R.J. Wang, Discrete unified gas kinetic scheme for all Knudsen number flows: low-speed isothermal case, Phys. Rev. E 88 (2013) 033305.
[10] J. Jiang, Y.H. Qian, Implicit gas-kinetic BGK scheme with multigrid for 3D stationary transonic high-Reynolds number flows, Comput. Fluids 66 (2012) 21–28.
[11] G.S. Jiang, C.W. Shu, Efficient implementation of Weighted ENO schemes, J. Comput. Phys. 126 (1996) 202–228.
[12] K.H. Kim, C. Kim, Accurate, efficient and monotonic numerical methods for multi-dimensional compressible flows. Part I: spatial discretization, J. Comput. Phys. 208 (2005) 527–569.
[13] L. Krivodonova, J. Xin, J.F. Remacle, N. Chevaugeond, J.E. Flahertyd, Shock detection and limiting with discontinuous Galerkin methods for hyperbolic conservation laws, Appl. Numer. Math. 48 (2004) 323–338.
[14] G. Kumar, S.S. Girimaji, J. Kerimo, WENO-enhanced gas-Kinetic scheme for direct simulations of compressible transition and turbulence, J. Comput. Phys. 234 (2013) 499–523.
[15] Q. Li, K. Xu, S. Fu, A high-order gas-kinetic Navier–Stokes flow solver, J. Comput. Phys. 229 (2010) 6715–6731.
[16] J. Luo, L.J. Xuan, K. Xu, Comparison of fifth-order WENO scheme and WENO-gas-kinetic scheme for inviscid and viscous flow simulation, Commun. Comput. Phys. 14 (2013) 599–620.
[17] J. Luo, K. Xu, A high-order multidimensional gas-kinetic scheme for hydrodynamic equations, Sci. China, Technol. Sci. 56 (2013) 2370–2384.
[18] L. Mieussens, On the asymptotic preserving property of the unified gas-kinetic scheme for the diffusion limit of linear kinetic models, J. Comput. Phys. 253 (2013) 138–156.
[19] T. Ohwada, K. Xu, The kinetic scheme for the full-Burnett equations, J. Comput. Phys. 201 (2004) 315–332.
[20] C.F. Ollivier-Gooch, Quasi-ENO schemes for unstructured meshes based on unlimited data-dependent least-square reconstruction, J. Comput. Phys. 133 (1997) 6–17.
[21] L. Pan, K. Xu, A compact third-order gas-kinetic scheme for compressible Euler and Navier–Stokes equations, Commun. Comput. Phys. 18 (2015) 985–1011.
[22] M. Pandolfi, D. D'Ambrosio, Numerical instabilities in upwind methods: analysis and cures for the "carbuncle" phenomenon, J. Comput. Phys. 166 (2001) 271–301.
[23] W. Sun, S. Jiang, K. Xu, An asymptotic preserving unified gas kinetic scheme for gray radiative transfer equations, J. Comput. Phys. 285 (2015) 265–279.
[24] P. Woodward, P. Colella, The numerical simulation of two dimensional fluids with strong shock, J. Comput. Phys. 54 (1984) 115–173.
[25] K. Xu, Direct Modeling for Computational Fluid Dynamics: Construction and Application of Unified Gas-kinetic Schemes, World Scientific, 2015.
[26] K. Xu, A gas-kinetic BGK scheme for the Navier–Stokes equations and its connection with artificial dissipation and Godunov method, J. Comput. Phys. 171 (2001) 289–335.
[27] K. Xu, J. Huang, A unified gas-kinetic scheme for continuum and rarefied flows, J. Comput. Phys. 229 (2010) 7747–7764.